Pure Appl. Geophys. 171 (2014), 361–375

DOI 10.1007/s00024-012-0573-6

Pure and Applied Geophysics

The IDC Seismic, Hydroacoustic and Infrasound Global Low and High Noise Models

David Brown,[1] Lars Ceranna,[2] Mark Prior,[1] Pierrick Mialle,[1] and Ronan J. Le Bras[1]

Abstract—The International Data Centre (IDC) in Vienna, Austria, is determining, as part of automatic processing, sensor noise levels for all seismic, hydroacoustic, and infrasound (SHI) stations in the International Monitoring System (IMS) operated by the Provisional Technical Secretariat of the Comprehensive Nuclear-Test-Ban Treaty Organization (CTBTO). Sensor noise is being determined several times per day as a power spectral density (PSD) using the Welch overlapping method. Based on accumulated PSD statistics a probability density function (PDF) is also determined, from which low and high noise curves for each sensor are extracted. Global low and high noise curves as a function of frequency for each of the SHI technologies are determined as the minimum and maximum of the individual station low and high noise curves, respectively, taken over the entire network of contributing stations. An attempt is made to ensure that only correctly calibrated station data contributes to the global noise models by additionally considering various automatic detection statistics. In this paper global low and high noise curves for 2010 are presented for each of the SHI monitoring technologies. Except for a very slight deviation at the microseism peak, the seismic global low noise model returns identically the Peterson (1993) NLNM low noise curve. The global infrasonic low noise model is found to agree with that of Bowman *et al.* (2005, 2007) but disagrees with the revised results presented in Bowman *et al.* (2009) by a factor of 2 in the calculation of the PSD. The global hydroacoustic low and high noise curves are found to be in quantitative agreement with Urick's oceanic ambient noise curves for light to heavy shipping. Whale noise is found to be a feature of the hydroacoustic high noise curves at around 15 and 25 Hz.

Key words: Seismic, infrasound, hydroacoustic, global noise models.

1. Introduction

The Provisional Technical Secretariat for the Preparatory Commission for the Comprehensive Nuclear-Test-Ban Treaty Organization is tasked with establishing the verification regime for the Comprehensive Nuclear-Test-Ban Treaty (CTBT) that, upon Entry Into Force (EIF), bans the detonation of nuclear devices in any environment. The framework of the verification regime is the global network of 337 seismic, hydroacoustic, infrasound, and radionuclide stations that form the International Monitoring System. The International Data Centre processes in near real time data received from the IMS stations, subsequently generating several event bulletins for the benefit of the States Parties that are signatories to the Treaty.

Along with its regular event processing, the IDC is also mandated to record and monitor station ambient noise with the expectation that knowledge of this sort may be indicative of station state of health (SOH).

Station ambient noise conditions are being represented by the power spectral density (PSD), which provides a measure of the power contained in the signal at each frequency.

Determining both single station and network low and high noise models becomes a straightforward procedure when station ambient noise information is routinely accessible. The purpose of this paper is to present the inferred global low and high noise models for each of the SHI technologies based on data recorded by the IMS network. In doing so, care is taken at all stages to ensure both the integrity of the data and the method used to determine the station noise information.

Section 2 of this paper discusses the method used in determining the station ambient noise, as well as

---

[1] International Data Centre, Comprehensive Nuclear-Test-Ban Treaty Organization, Preparatory Commission, IDC/CTBTO Vienna International Centre, PO Box 1200, 1400 Vienna, Austria. E-mail: David.Brown@ctbto.org

[2] Bundesanstalt für Geowissenschaften und Rohstoffe (BGR), Geozentrum Hannover Stilleweg 2, 30655 Hannover, Germany.

Birkhäuser

tests performed to ensure that the chosen PSD method is providing the correct estimation of the PSD.

Section 3 discusses the data used during the analysis, and section four the results for each of the SHI technologies.

2. *Numerical Method and Testing*

2.1. *Numerical Method*

The Welch overlapping method (Welch 1967) forms the basis of the procedure used in this paper to determine the PSD. In this method the time interval spanning the data under consideration is divided into a sequence of overlapping sub-intervals and the PSD for each sub-interval is determined. The average of the sub-interval PSD's is assumed to provide an estimate of the required PSD. This averaging procedure reduces the variance on the estimated PSD, which may otherwise be of the order of the contributing sample values (Welch 1967). Strictly speaking, the use of the PSD requires that the waveform under consideration be a Wide-Sense Stationary Process (see, e.g., Schreier and Scharf 2010), implying that both the mean and autocorrelation of the sampled waveform are time independent, in which case the PSD is the Fourier transform of the autocorrelation function as asserted by the Wiener–Khinchin theorem. Here we are assuming that stationarity is assumed to hold as the propagating signals are considered to be short-lived transitory phenomenon and will thus provide an only minor impact on the statistics.

When evaluating the PSD's, careful attention has been given to the spectral windowing process, which is discussed more fully in the Appendix. In this analysis we have chosen to use the nutall4a window of Heinzel *et al.* (2002), which is a good general purpose spectral window with spectral leakage properties superior to that of the Hanning or Hamming windows.

The PSD estimate used in this paper is given by the expression $P_{\mathrm{SD}}(\omega_j) = \frac{2\left|F(\omega_j)\right|^2}{\Delta I_W}$—where $\omega_j = \frac{2\pi j}{n\Delta}$ for $j = 0,\ldots,n/2$ is the jth frequency picket, n is the number of samples, Δ is the sample rate, F is the output of a unitary Fourier Transform algorithm and I_{w} the sum of the squares of the spectral window coefficients. This expression is discussed further in the Appendix and derived more fully in references like Harris (1978), and Heinzel *et al.* (2002).

2.2. *Testing*

Two levels of testing have been applied to the algorithm described in Sect. 2.1. The first is against an artificial dataset intended to mimic digitizer noise for which the PSD has a theoretically determinable expression. The second is a blind test with a second algorithm on an otherwise random selected data set.

2.2.1 *Test 1: Digitizer Noise*

The procedure described in Heinzel *et al.* (2002) has been used to test the algorithm. Here, each sample in a synthetic time-series data set has been rounded to multiples of a parameter U_0 defined a priori, which represents the least-significant-bit of a digitizer. In this case, the PSD has a noise-floor that is given by the expression (see, e.g., Lyons 1997) $U^2(\omega) = \frac{U_0^2}{6\Delta}$, where ω is angular frequency.

The following strategy outlined in Heinzel *et al.*, (2002) was used to generate the synthetic time-series data set:

1. The double-sinusoid $u(t) = A_1\sin(2\pi f_1 t) + A_2\sin(2\pi f_2 t)$ is used to provide the basic analogue signal. Here, $f_1 = 0.3123456$ Hz, $f_2 = 2.0$ Hz, $A_1 = 2.123456$, $A_2 = 1.0$ is used.
2. $u(t)$ has been sampled at 20 Hz to provide the time-series: $u_j = A_1\sin\left(\frac{2\pi f_1 j}{\Delta}\right) + A_2\sin\left(\frac{2\pi f_2 j}{\Delta}\right)$ for $j = 1,\ldots,N$.
3. The new time-series $y_j$for $j = 1,\ldots,N$ is formed, where $y_j = \mathrm{int}\left[\frac{u_j}{U_0} + 0.5\right]U_0$.
4. With the values for A_1, A_2, f_1, f_2, $U_{0,}$ and Δ as given above we should expect a white noise background with $\log_{10}\mathrm{PSD} = \log_{10}\left(\frac{U_0}{6\Delta}\right) = -8.079$.

With this procedure a time-series with duration 1-h was generated. After passing the algorithm as described above over the synthetic data set, the PSD as shown in Fig. 1 was obtained.

The desired noise floor is accurately rendered, and further, when multiplying by the Equivalent Noise Bandwidth for the nutall4a window (see the

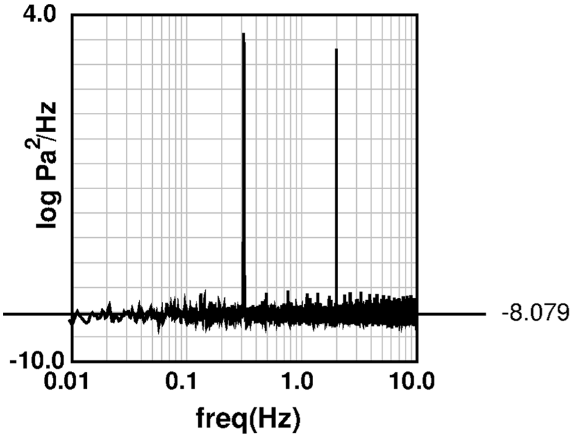

Figure 1
Power spectral density as a function of frequency for the Test 1 data set

Appendix), the amplitude of the spectral peaks is accurately determined, as is shown in Fig. 1.

2.2.2 *Test 2: Blind Test with a Second Independent PSD Algorithm*

One-hour data segments were chosen randomly from the list of infrasound stations provided in Table 1. A completely independent second algorithm that uses the matlab *pwelch* function (Matlab 2008) to estimate PSD's (denoted as BGR in what follows) was provided by one of the authors and compared with the algorithm described above (denoted CTBTO in what follows). The results are shown in Fig. 2 and indicate excellent agreement.

We conclude from these two tests that the algorithm is functioning, as it should.

3. *The Data*

The IMS seismic, hydroacoustic and infrasound stations that were used in the current analysis are listed in Table 1; the locations of the stations is shown in Fig. 3.

Both primary and auxiliary seismic stations were used in this analysis, and although data from the primary stations is continuously recorded, the auxiliary stations generally send data upon request in order to refine knowledge of a seismic event during the analysis stage. Data from the auxiliary seismic stations may therefore not be present for the entire analysis period.

Data sampled four times per day for the whole of 2010 were used in the current analysis except in situations where better resolution of the low or high noise models was required for a particular station where the data was sampled each hour for the entire year.

Each sampling consisted of 1-h of waveform data divided into 3-min overlapping segments as outlined above, with the seismic data being deconvolved to acceleration and the infrasound and hydroacoustic data deconvolved to displacement, the instrument response has been removed in each case. Note that in the case of the infrasound data only the response of the sensor and digitizer has been removed, not that of the spatial filter system that was likely to be present.

4. *Low and High Noise Models*

Probability Density Functions using the procedure discussed by McNamara and Buland (2004) are determined for each SHI sensor. Data displayed in this format allows a ready estimate of the sensor low and high noise models for the period in which data was contributed. As an example, Fig. 4 shows the PDF obtained for sensor I02AR/I02H1 for the year 2010. The low and high noise curves as a function of frequency are determined by plotting the PDF function at the 5 and 95 % probability levels, respectively. The global low noise curve as a function of frequency is defined to be, for a given frequency, the minimum of the low noise curves from all contributing sensors across all stations at the given frequency. Only stations with sufficient contributing data such that a well-defined PDF is formed with well-behaved low and high noise curves were used in the analysis.

4.1. *Seismic*

A random shift of up to 6 h is applied to the requested processing time for the seismic data in order to reduce the likelihood of contamination by regular cultural noise. Only vertical channels were considered when performing the seismic analysis,

Table 1

IMS seismic, hydroacoustic and infrasound stations that were used in the current analysis

Station	Location	State	Latitude	Longitude	Station type
AKASG	Malin	Ukraine	50.7012	29.2242	Primary seismic
ARCES	Finnmark	Norway	69.5348	25.5057	Primary seismic
ASAR	Alice Springs	Australia	−23.665134	133.90526	Primary seismic
BDFB	Brasilia	Brazil	−15.64178	−48.01485	Primary seismic
BOSA	Boshof	South Africa	−28.61405	25.25542	Primary seismic
BRTR	Belbashi	Turkey	39.725	33.639	Primary seismic
CMAR	Chiang Mai	Thailand	18.4576	98.94315	Primary seismic
CPUP	Villa Florida	Paraguay	−26.3307	−57.331	Primary seismic
DBIC	Dimbroko	Cote d'Ivoire	6.6701	−4.8563	Primary seismic
ESDC	Sonseca	Spain	39.6744	−3.963	Primary seismic
FINES	Lahti	Finland	61.4436	26.0771	Primary seismic
GERES	Freyung	Germany	48.845106	13.701559	Primary seismic
GEYT	Alibeck	Turkmenistan	37.92955	58.11706	Primary seismic
ILAR	Eielson	United States of America	64.771446	−146.88665	Primary seismic
KBZ	Khabaz	Russian Federation	43.726898	42.8996	Primary seismic
KEST	Kesra	Tunisia	35.7317	9.346	Primary seismic
KMBO	Kilimambogo	Kenya	−1.1268	37.2523	Primary seismic
KSRS	Wonju	Republic of Korea	37.4421	127.8844	Primary seismic
LPAZ	La Paz	Bolivia	−16.287927	−68.130706	Primary seismic
MAW	Mawson Antarctica	Australia	−67.6046	62.8713	Primary seismic
MJAR	Matushiro	Japan	36.524717	138.24718	Primary seismic
MKAR	Makanchi	Kazakhstan	46.7937	82.2904	Primary seismic
NOA	Hamar	Norway	61.0397	11.2148	Primary seismic
NVAR	Mina Nevada	United States of America	38.429609	−118.30355	Primary seismic
PDAR	Pinedale Wyoming	United States of America	42.7667	−109.5579	Primary seismic
PETK	Petropavlovsky-Kamchatskiy	Russian Federation	53.108215	157.69885	Primary seismic
PLCA	Paso Flores	Argentina	−40.732733	−70.550835	Primary seismic
PPT	Tahiti	France	−17.5896	−149.5764	Primary seismic
ROSC	El Rosal	Columbia	4.844856	−74.321203	Primary seismic
SCHQ	Schefferville Quebec	Canada	54.832402	−66.833177	Primary seismic
SONM	Songino	Mongolia	47.83469	106.39499	Primary seismic
STKA	Stephens Creek	Australia	−31.8743	141.5964	Primary seismic
TORD	Torodi	Niger	13.14771	1.6947087	Primary seismic
TXAR	Lajitas Texas	United States of America	29.333965	−103.66769	Primary seismic
ULM	Lac Du Bonnet, Manitoba	Canada	50.250261	−95.874956	Primary seismic
USRK	Ussuriysk	Russian Federation	44.1998	131.9888	Primary seismic
VNDA	Vanda, Antarctica	United States of America	−77.5173	161.8528	Primary seismic
WRA	Warramunga NT	Australia	−19.942589	134.33951	Primary seismic
YKA	Yellowknife	Canada	62.4931	−114.6062	Primary seismic
ZALV	Zalesovo	Russian Federation	53.948063	84.818807	Primary seismic
AAK	Ala-Archa	Kyrgyzstan	42.6391	74.4942	Auxiliary seismic
AFI	Afiamalu	Samoa	−13.9093	−171.7773	Auxiliary seismic
AKTO	Aktyubinsk	Kazakhstan	50.4348	58.0164	Auxiliary seismic
ANMO	Albuquerque, New Mexico	United States of America	34.9462	−106.4567	Auxiliary seismic
ASF	Tel Al Asfar	Jordan	32.1723	36.8972	Auxiliary seismic
ATAH	Atahualpa	Peru	−7.13506	−78.39445	Auxiliary seismic
ATD	Arta Tunnel	Djibouti	11.53	42.847	Auxiliary seismic
BATI	Baumata, Nusa Tengarra	Indonesia	−10.206	123.6627	Auxiliary seismic
BBB	Bella Bella	Canada	52.1847	−128.1133	Auxiliary seismic
BBTS	Babate	Senegal	14.6604	−16.5334	Auxiliary seismic
BORG	Borganes	Iceland	64.7474	−21.3268	Auxiliary seismic
BVAR	Borovoye	Kazakhstan	53.0249	70.3885	Auxiliary seismic
CFAA	Coronel Fontana	Argentina	−31.60475	−68.23756	Auxiliary seismic
CMIG	Colonia Cuauhtemoc, Oaxaca	Mexico	17.091	−94.8838	Auxiliary seismic
CTA	Charters Towers	Australia	−20.0876	146.25	Auxiliary seismic

Table 1 *continued*

Station	Location	State	Latitude	Longitude	Station type
DAVOX	Davos	Switzerland	46.7806	9.8797	Auxiliary seismic
DLBC	Dease Lake, British Columbia	Canada	58.43696	−130.03051	Auxiliary seismic
DZM	Mont Dzumad	New Caledonia	−22.068	166.4469	Auxiliary seismic
EIL	Eilath	Israel	29.6725	34.9519	Auxiliary seismic
EKA	Eskdalemuir	United Kingdom	55.3332	−3.1588	Auxiliary seismic
ELK	Elko, Nevada	United States of America	40.7448	−115.2388	Auxiliary seismic
FITZ	Fitzroy Crossing	Australia	−18.09826	125.6403	Auxiliary seismic
FRB	Iqaluit	Canada	63.7467	−68.5467	Auxiliary seismic
GNI	Garni	Armenia	40.1495	44.7414	Auxiliary seismic
GUMO	Guam, Marianas Islands	United States of America	13.5892	144.8684	Auxiliary seismic
HFS	Hagfors	Sweden	60.133474	13.69449	Auxiliary seismic
HNR	Honiara	Solomon Islands	−9.4322	159.9471	Auxiliary seismic
IDI	Anóyia	Greece	35.288	24.89	Auxiliary seismic
INK	Inuvik, Northwest Territory	Canada	68.306516	−133.52543	Auxiliary seismic
JCJ	Chichijima, Ogasawara	Japan	27.095467	142.18463	Auxiliary seismic
JKA	Kamikawa-Asahi, Hokkaido	Japan	44.11895	142.59325	Auxiliary seismic
JMIC	Jan Mayen	Norway	70.9866	−8.50515	Auxiliary seismic
JNU	Ohita, Kyushu	Japan	33.121667	130.87833	Auxiliary seismic
JOW	Kunigami, Okinawa	Japan	26.836	128.2731	Auxiliary seismic
JTS	Las Juntas de Abangares	Costa Rica	10.2908	−84.9525	Auxiliary seismic
KAPI	Kappang, Sulawesi	Indonesia	−5.0142	119.7517	Auxiliary seismic
KDAK	Kodiak Island, Alaska	United States of America	57.7828	−152.5835	Auxiliary seismic
KURK	Kurchatov	Kazakhstan	50.62264	78.53039	Auxiliary seismic
KVAR	Kislovodsk, Stavropol'skiy	Russian Federation	43.9557	42.6952	Auxiliary seismic
LBTB	Lobatse	Botswana	−25.0151	25.5966	Auxiliary seismic
LEM	Lembang, Jawa Barat	Indonesia	−6.82645	107.61748	Auxiliary seismic
LPIG	La Paz, Baja California Sur	Mexico	24.10103	−110.30931	Auxiliary seismic
LSZ	Lusaka	Zambia	−15.2766	28.1882	Auxiliary seismic
MATP	Matopo	Zimbabwe	−20.42583	28.49944	Auxiliary seismic
MBAR	Mbarara	Uganda	−0.6019	30.7382	Auxiliary seismic
MDT	Midelt	Morocco	32.814	−4.607	Auxiliary seismic
MLR	Muntele Rosu	Romania	45.4917	25.9437	Auxiliary seismic
MMAI	Mount Meron	Israel	33.01518	35.40311	Auxiliary seismic
MSKU	MasUnited Kingdomu	Gabon	−1.6557	13.6116	Auxiliary seismic
NEW	Newport, Washington	United States of America	48.26333	−117.12	Auxiliary seismic
NNA	Nana	Peru	−11.9873	−76.8422	Auxiliary seismic
NWAO	Narrogin	Australia	−32.9277	117.239	Auxiliary seismic
OBN	Obninsk	Russian Federation	55.1138	36.5687	Auxiliary seismic
OPO	Ambohidratompo	Madagascar	−18.5706	47.1879	Auxiliary seismic
PALK	Pallekele	Sri Lanka	7.2728	80.7022	Auxiliary seismic
PCRV	Puerto la Cruz	Venezuela	10.1634	−64.58963	Auxiliary seismic
PFO	Pinon Flat, California	United States of America	33.6092	−116.4553	Auxiliary seismic
PMG	Port Moresby	Papua New Guinea	−9.4092	147.1539	Auxiliary seismic
PMSA	Palmer Station, Antarctica	United States of America	−64.7742	−64.049	Auxiliary seismic
PSI	Parapat, Sumatra	Indonesia	2.6952	98.924	Auxiliary seismic
QSPA	South Pole, Antarctica	United States of America	−89.9279	145.0	Auxiliary seismic
RAO	Raoul, Kermadec Islands	New Zealand	−29.2517	−177.9183	Auxiliary seismic
RAR	Raratonga	Cook Islands	−21.2125	−159.7733	Auxiliary seismic
RCBR	Riachuelo	Brazil	−5.82739	−35.90131	Auxiliary seismic
RES	Resolute, Nunavut	Canada	74.689233	−94.896167	Auxiliary seismic
RPN	Easter Island	Chile	−27.1267	−109.3344	Auxiliary seismic
RPZ	Rata Peaks	New Zealand	−43.7146	171.054	Auxiliary seismic
SADO	Sadowa	Canada	44.7694	−79.1417	Auxiliary seismic
SEY	Seymchan	Russian Federation	62.9328	152.3822	Auxiliary seismic
SFJD	Søndre Strømford	Greenland	66.995999	−50.6215	Auxiliary seismic
SIV	San Ignacio	Bolivia	−15.991	−61.072	Auxiliary seismic
SJG	San Juan	Puerto Rico	18.1117	−66.15	Auxiliary seismic

Table 1 *continued*

Station	Location	State	Latitude	Longitude	Station type
SNAA	Sanae Station, Antarctica	Germany/South Africa	−71.6707	−2.8379	Auxiliary seismic
SPITS	Spitsbergen	Norway	78.1777	16.37	Auxiliary seismic
SUR	Sutherland	South Africa	−32.3797	20.8117	Auxiliary seismic
TEIG	Tepich, Yucatan	Mexico	20.2264	−88.2776	Auxiliary seismic
TGY	Tagatay City	Philippines	14.1008	120.93837	Auxiliary seismic
TKL	Tuckaleechee Caverns, Tennessee	United States of America	35.658	−83.774	Auxiliary seismic
TSUM	Tsumeb	Namibia	−19.2022	17.5838	Auxiliary seismic
URZ	Urewera	New Zealand	−38.2592	177.1109	Auxiliary seismic
USHA	Ushuaia	Argentina	−54.83192	−68.43432	Auxiliary seismic
VAE	Valguarnera	Italy	37.469	14.3533	Auxiliary seismic
VRAC	Vranov	Czech Republic	49.30828	16.59351	Auxiliary seismic
YBH	Yreka Blue Horn	United States of America	41.73193	−122.71038	Auxiliary seismic
I02AR	Ushuaia	Argentina	−54.58057	−67.30923	Infrasound
I04AU	Shannon	Australia	−34.59761	116.35669	Infrasound
I05AU	Hobart	Australia	−42.490798	147.68063	Infrasound
I07AU	Warramunga NT	Australia	−19.93482	134.32953	Infrasound
I08BO	Penas-Bolivia	Bolivia	−16.21523	−68.45345	Infrasound
I09BR	Brasilia	Brazil	−15.637967	−48.016422	Infrasound
I10CA	Lac Du Bonnet	Canada	50.201469	−96.026854	Infrasound
I11CV	Maio	Cape Verde	15.25729	−23.18388	Infrasound
I13CL	Easter Island	Chile	−27.12726	−109.36265	Infrasound
I14CL	Robinson Carusoe Island	Chile	−33.65379	−78.79598	Infrasound
I17CI	Dimbokro	Ivory Coast	6.6703566	−4.8569106	Infrasound
I18DK	Qaanaaq	Greenland	77.47556	−69.28776	Infrasound
I21FR	Marquesas Islands	France	−8.86783	−140.15907	Infrasound
I22FR	Port Laguerre New Caldeonoia	FRANCE	−22.18445	166.84592	Infrasound
I23FR	Kerguelen	France	−49.34578	70.24159	Infrasound
I24FR	Tahiti	France	−17.74929	−149.29582	Infrasound
I26DE	Freyung	Germany	48.851617	13.713128	Infrasound
I27DE	Georg von Neumayer Antarctica	Germany	−70.7011	−8.30291	Infrasound
I30JP	Isumi	Japan	35.307756	140.31376	Infrasound
I31KZ	Aktyubinsk	Kazakhstan	50.40697	58.03482	Infrasound
I32KE	Nairobi	Kenya	−1.24216	36.82721	Infrasound
I33MG	Antananarivo	Madagascar	−19.010859	47.305024	Infrasound
I34MN	Songino	Mongolia	47.80172	106.41012	Infrasound
I35NA	Tsumeb	Namibia	−19.19135	17.57678	Infrasound
I36NZ	Chatham Islands	New Zealand	−43.91662	−176.48337	Infrasound
I39PW	Palau	Palau	7.53547	134.54704	Infrasound
I41PY	Villa Florida	Paraguay	−26.3423	−57.31188	Infrasound
I43RU	Dubna	Russian Federation	56.72136	37.21759	Infrasound
I44RU	Petropavlovsk-Kamchatsky	Russian Federation	53.1058	157.7139	Infrasound
I45RU	Ussuriysk	Russian Federation	44.1999	131.9773	Infrasound
I46RU	Zalesovo	Russian Federation	53.94872	84.81891	Infrasound
I47ZA	Boshof	South Africa	−28.621123	25.235228	Infrasound
I48TN	Kesra	Tunisia	35.80523	9.32302	Infrasound
I49 GB	Tristan Da Cunha	United Kingdom	−37.08995	−12.33192	Infrasound
I50 GB	Ascension Island	United Kingdom	−7.93774	−14.37517	Infrasound
I51 GB	Bermuda	United Kingdom	32.36154	−64.69874	Infrasound
I52 GB	Diego Garcia	United Kingdom	−7.37781	72.484161	Infrasound
I53US	Fairbanks Alaska	United States of America	64.875	−147.86114	Infrasound
I55US	Windless Bight Antarctica	United States of America	−77.73149	167.58742	Infrasound
I56US	Newport Washington	United States of America	48.26408	−117.12567	Infrasound
I57US	Pinon Flat California	United States of America	33.605852	−116.45328	Infrasound
I59US	Hawaii	United States of America	19.591532	−155.8936	Infrasound
H01	Cape Leeuwin	Australia	−34.88316	114.13608	Hydroacoustic
H03	Juan Fernandez Island	Chile	−33.825843	−78.909483	Hydroacoustic
H08	Diego Garcia	United Kingdom	−7.6275	72.48383	Hydroacoustic

Table 1 *continued*

Station	Location	State	Latitude	Longitude	Station type
H10	Ascension Island	United Kingdom	−8.95274	−14.6629	Hydroacoustic
H11	Wake Island	United States of America	18.49568	166.68646	Hydroacoustic

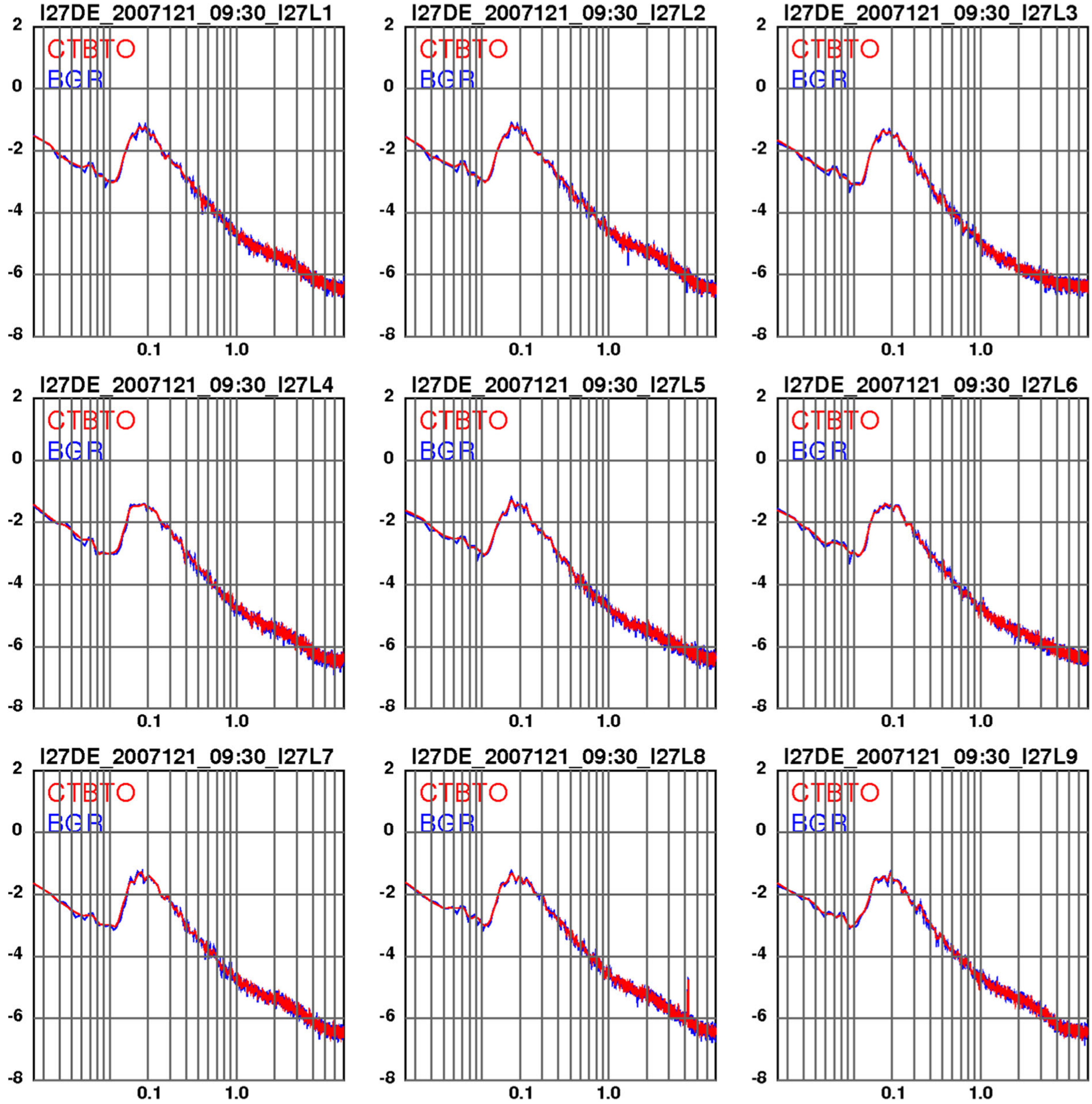

Figure 2

Results of a blind-comparison test between two different PSD algorithms on randomly chosen infrasound data. Abscissa values are frequency in Hz, and ordinate values are logarithm base 10 of the PSD in Pa^2 per Hz. The CTBTO data refer to results generated by the procedure discussed in this Paper. The BGR data refers to a second independent algorithm provided by one of the present authors

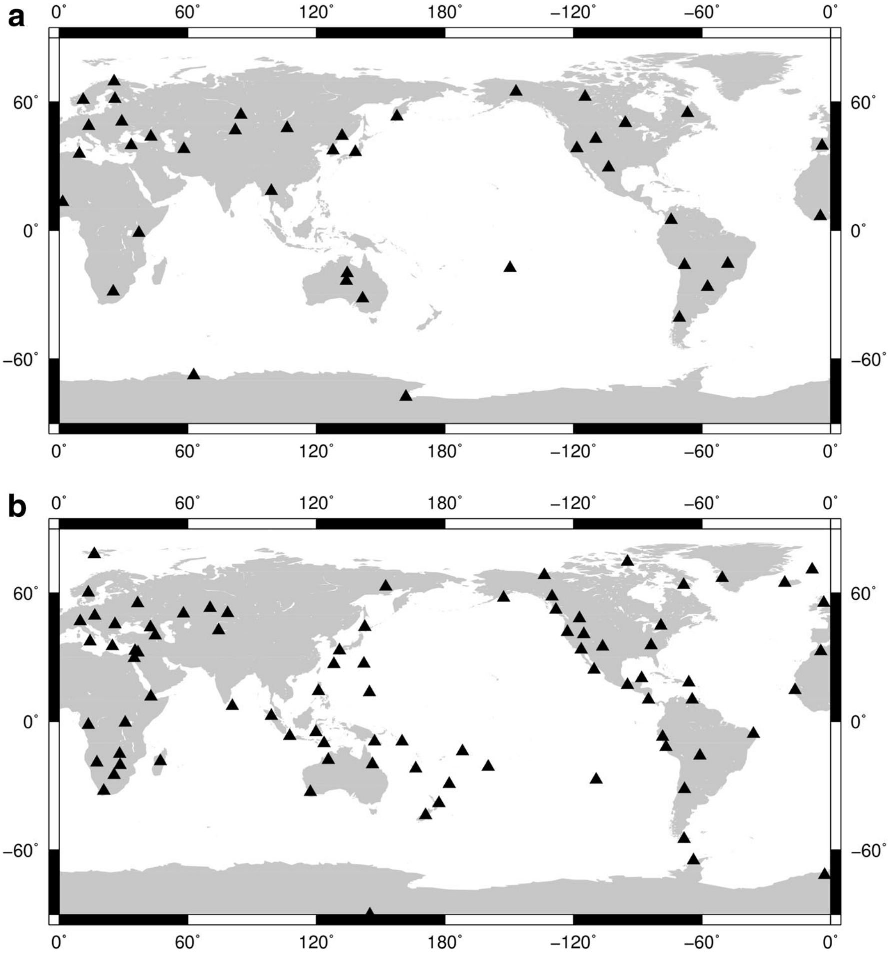

Figure 3

a Location of the primary seismic stations that contributed to the present analysis. **b** Location of the auxiliary seismic stations that contributed to the present analysis. **c** Location of the primary infrasound stations that contributed to the present analysis. **d** Location of the primary hydroacoustic stations that contributed to the present analysis. Note that no T-stations were used in this component of the present analysis

and, in the case of short-period seismic sensors, only spectral data at frequencies higher than 0.1 Hz were allowed to contribute to the analysis.

Event bulletins can be used as an additional measure to ensure that correctly calibrated data are contributing to the seismic low and high noise models. Event mb and Ms magnitude residuals (i.e., network magnitude estimate minus the station magnitude estimate) were plotted as a function of time for each station for the time duration under consideration and a station allowed to contribute to the global noise models if the Ms and mb magnitude residuals were less than 0.3 magnitude units. An example of a station with data that is correctly calibrated and unlikely to bias the global noise models is shown in Fig. 5. An example of a station with data that may have a calibration error and could bias the global noise models if used is shown in Fig. 6.

The IDC global seismic low and high noise curves for 2010, referred to here as *IDC2010_LS* and *IDC2010_HS*, respectively, are shown in Fig. 7. Also shown for comparison are the NLNM and NHNM curves from Peterson (1993). The IDC2010_LS and NLNM curves are in good agreement, particularly in the low noise case. The microseism peak is slightly lower in the case of the IDC2010_LS model; station AAK (Ala Archa, Kyrgyzstan) was found to be

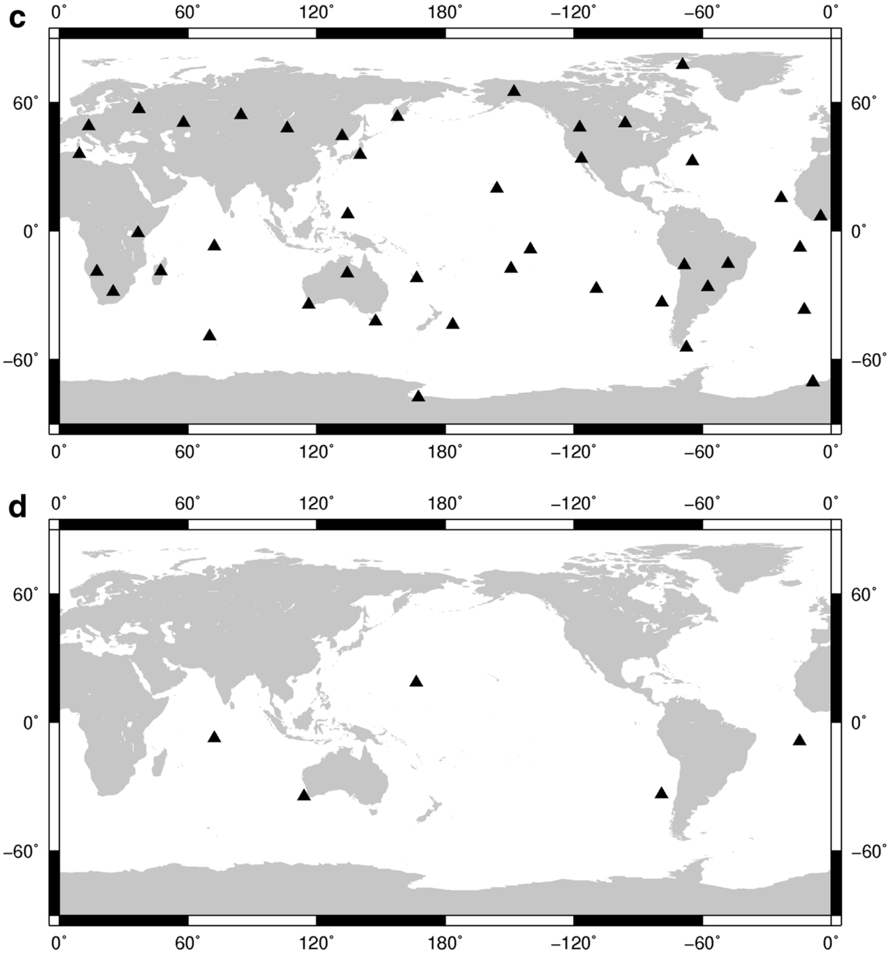

Figure 3
continued

largely responsible for this slight deviation. In order to better resolve the contribution of this station to the low noise curve, data for the entire year, i.e., every hour in the day, for station AAK was processed.

Fairly good agreement exists between IDC2010_HS and the NHNM. The microseismic peak is slightly elevated in the IDC2010_HS model compared to the NHNM model, which is found to be due largely to station BORG (Borgarfjordur, Asbjarnarstadir, Iceland). This station commenced operation in 1994, so it would not have contributed to the Peterson (1993) analysis. Waveform data for stations BORG was computed each hour for the entire year to better resolve its contribution to the IDC2010_HS model.

4.2. *Hydroacoustic*

Once again a random time shift of up to 6 h is applied to the requested processing time in order to reduce contamination from regular cultural noise.

The IDC global hydroacoustic low and high noise curves for 2010, referred to here as *IDC2010_LH* and *IDC2010_HH*, respectively, are shown in Fig. 8. Stations that contributed to these curves are shown in Fig. 3d. No T-stations were used during this analysis, so only in-water hydroacoustic signals contributed to the global noise curves. The low and high noise curves differ by a constant 20 dB from 0.01 Hz to around 6 Hz where the low noise curve begins to register shipping noise, making the curve relatively

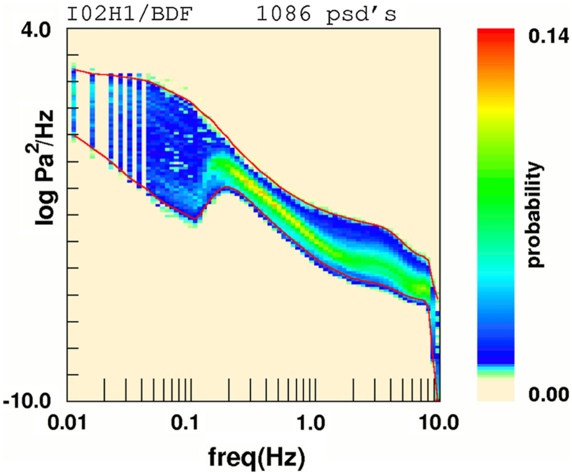

Figure 4
The PDF obtained for sensor I02AR/I02H1 for the year 2010. The *low and high noise curves* as shown in *red* are determined by plotting the PDF function at the 5 and 95 % probability levels, respectively

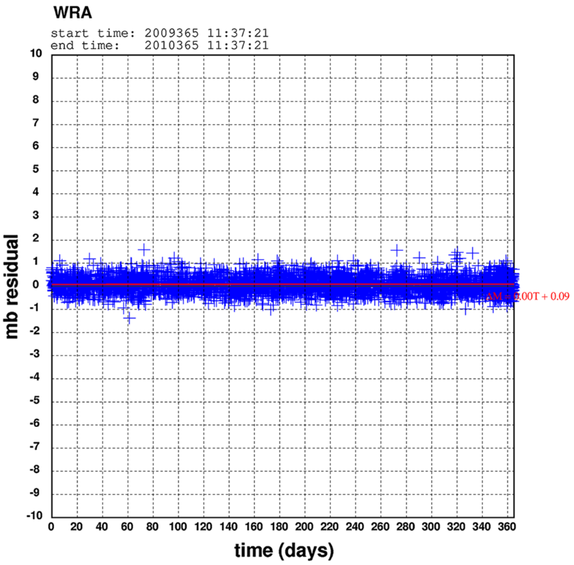

Figure 5
Event mb magnitude residual as a function of time for station WRA during 2010. No bias exists in the magnitude estimate suggesting the calibration for this station is correct

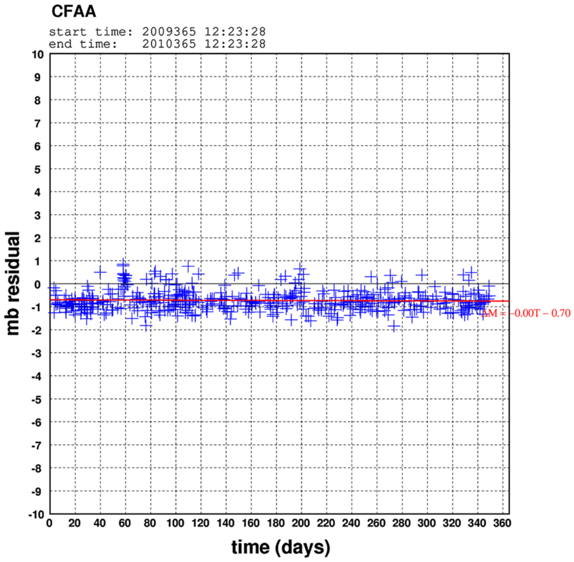

Figure 6
Event mb magnitude residual as a function of time for station CFAA during 2010. A clear bias of around −0.7 magnitude units exists for this station suggests a calibration error. The *red line* is the line of best fit through the data

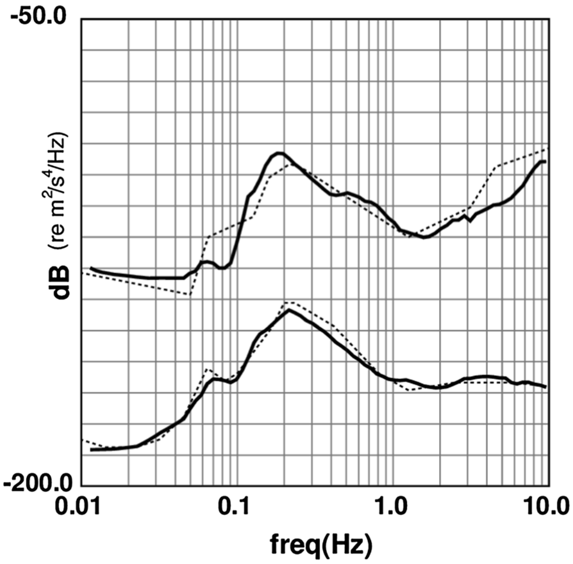

Figure 7
The global seismic low noise model IDC2010_LS and high noise model IDC2010_HS (*solid lines*) compared with the NHNM and NLNM of Peterson (1993) (*dashed lines*)

flat out to around 100 Hz. The microseismic peak at around 5 s period is clearly visible in both curves. It is worth noting that the microseismic energy is being measured directly in the water, which means that it is a more local measurement of surface wave activity than for seismic stations that receive microseism energy from a large area of ocean after propagating through the crust. This explains why the low noise and high noise curves exhibit the same microseismic deviation. Also shown in Fig. 8 for comparison are the oceanic ambient noise curves presented in Urick

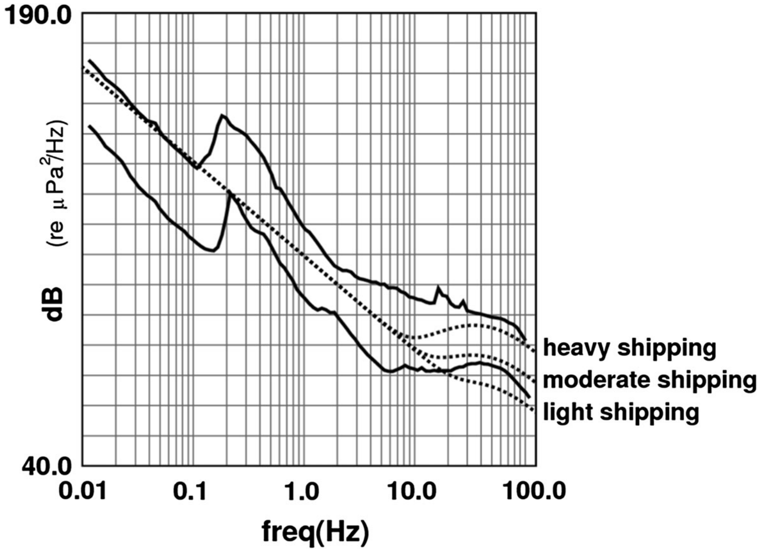

Figure 8
The global hydroacoustic low noise model IDC2010_LH and high noise model IDC2010_HH (*solid curves*) with Urick's noise curves superimposed (Urick 1984) for light, moderate and heavy shipping (*dashed curves*). Note that the wind component in the Urick curves was assumed to be zero, as the contribution due to the wind is not particularly significant below 100 Hz

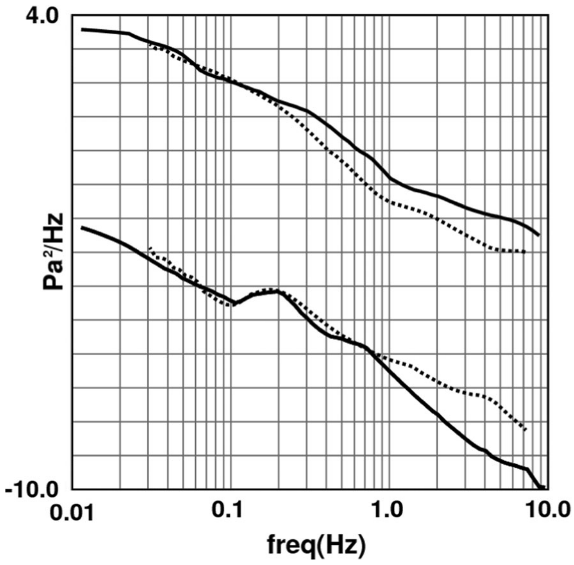

Figure 9
The global infrasonic low noise model IDC2010_LI and high noise model IDC2010_HI (*solid lines*) compared with a two times scaled version of the Bowman (2009) that can be assumed to be representative of the Bowman (2005, 2007) values (*dashed lines*)

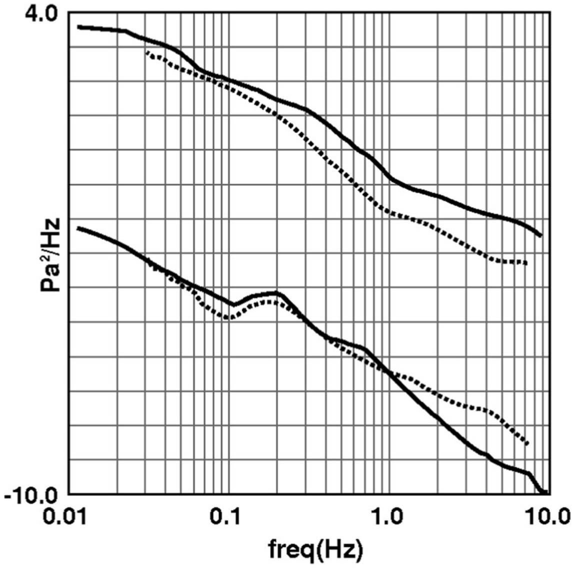

Figure 10
The global infrasonic low noise model IDC2010_LI and high noise model IDC2010_HI (*solid lines*) compared with those of Bowman (2009) (*dashed lines*)

(1984) for light to heavy shipping. Good quantitative agreement is observed to exist between these two sets of curves. The features in the high noise curve at around 15 and 25 Hz are likely to be due to blue and fin whale calling (see, e.g., McCauley *et al.*, 2001; Richardson *et al.* 1995).

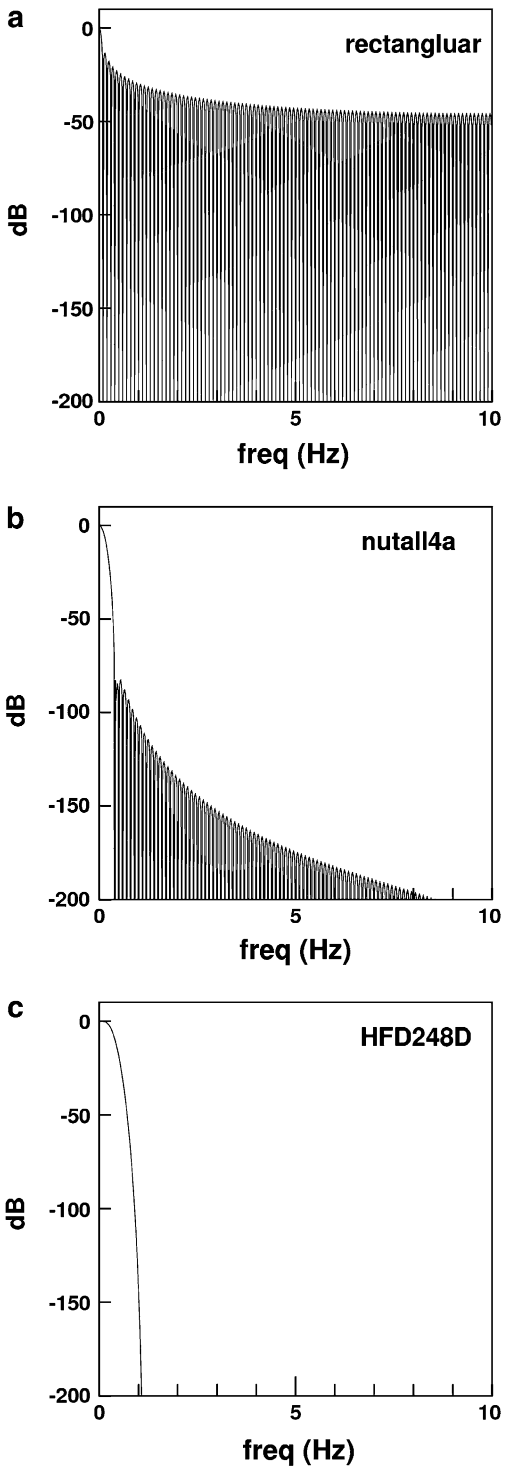

Figure 11
Transform of three spectral windows: **a** rectangular; **b** nutall4a; **c** HFD248D. See Heinzel *et al.* (2002) for a discussion on these last two windows

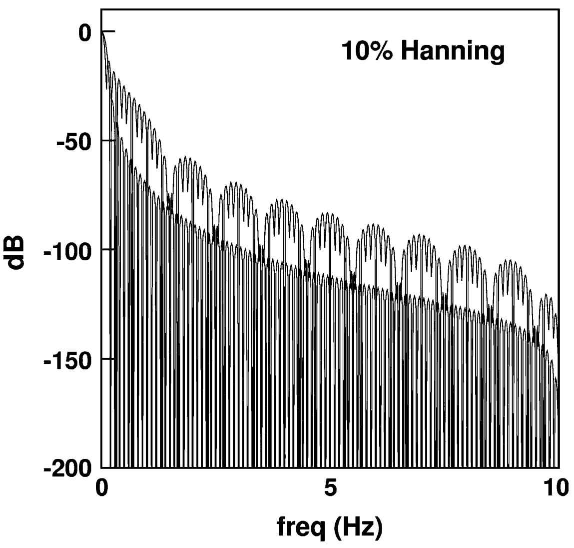

Figure 12
Transform of window function with a Hanning taper applied to the outer 10 % of the window and with the inner 80 % of the window function set to unity (*upper curve*). The transform of the usual Hanning window is also shown for comparison (*lower curve*)

4.3. Infrasonic

Infrasound data is requested at the local time: 03:30–04:30, 09:30–10:30, 15:30–16:30 and 21:30–22:30 at each recording station in order to sample the coldest part of the night (~4 am) and warmest part of the day (~4 pm), although it is appreciated these times may become a fairly inaccurate approximation for stations with extreme latitudes.

During the formulation of these noise curves station IS23, located at Kerguelen, was dropped from the high noise analysis as strong resonance peaks generated by the spatial filters significantly elevated the Power Spectral Densities at high frequencies, and would lead to a bias in the global high noise model.

The IDC global infrasonic low and high noise curves for 2010, referred to here as *IDC2010_LI* and *IDC2010_HI*, respectively, are shown in Fig. 9. Also shown in Fig. 9 are the global low and high infrasonic noise curves reported by Bowman *et al.* (2009) that have been scaled by two in the PSD's and can be assumed to be representative of the 2005/2007 results, since Bowman *et al.* (2009) state their 2009 results differ from the earlier 2005/2007 results by a factor of two, the latter results being half of the earlier results. The revised noise curves presented in Bowman *et al.* (2009) are shown in Fig. 10. Inspection shows that the Bowman (2005, 2007) low noise curves and IDC2010_LI curve are in close agreement around the microbarom peak. The IDC2010_LI curve drops below the Bowman curve at higher frequencies. This is due to the inclusion of station IS55 in the IDC2010_LI curve where it was excluded from the Bowman analysis. Station IS55, located at Windless Bight in the Antarctic, employs sensors manufactured by Chaparral Physics that are known to have very low self-noise at high frequencies. This station was excluded in the Bowman analysis because the authors felt that snow covering the spatial filters may artificially lower the recorded noise levels. However, it was included in this analysis as it is thought that the Chaparral sensors make an important contribution to the high frequency end of the noise curves that would otherwise be ignored. It is felt here that the curve obtained with the IS55 sensors included would more likely be closer to reality than those obtained leaving them out. The revised noise curves presented in Bowman *et al.* (2009) shown in Fig. 10 are consistently out in the value of the PSD's by a factor of 2, suggesting from this analysis that the original analysis of Bowman *et al.* (2005, 2007) is correct and a systematic error was introduced in the more recent work.

5. *Conclusions*

Data recorded in 2010 from the CTBTO IMS seismic, hydroacoustic and infrasound networks has been used to infer global low and high ambient noise curves.

The determined seismic global low and high noise curves are found to be in excellent agreement with those established by Peterson (1993), whereas the global infrasound low and high noise curves are found to be in general agreement with the Bowman (2005, 2007) models, but disagree with the revised models presented in Bowman (2009), which seem to have a factor of 2 error in the determination of the PSD. The hydroacoustic global low and high noise curves both exhibit contributions from the microseisms at low frequencies and shipping noise at high frequencies. Whale noise is a feature of the high noise curve at 15 and 25 Hz.

Acknowledgments

The authors would like to thank Dr. Roger Bowman for providing copies of his infrasound global noise models.

Disclaimer The views expressed in this paper are those of the authors and do not necessarily reflect those of the Preparatory Commission.

Appendix: Estimation of the Power Spectral Density

The selection of a finite-time interval of digitally sampled data, with supposedly constant sample rate, is equivalent to taking the analogue signal and applying two processes:

1. Sampling using the periodic Dirac Comb function $D(t) = \sum_{k=-\infty}^{\infty} \delta(t - kT)$, where T is the sampling period
2. Windowing using the box-car window function $w(t) = \begin{cases} 1 & \text{when } 0 \leq t \leq KT \\ 0 & \text{otherwise} \end{cases}$, where it is assumed that time zero is at the beginning of the box-car function, which is of duration *KT*.

The Fourier transform now becomes:

$$F(f(t)D(t)w(t)) \equiv F(\omega) * D(\omega) * W(\omega) \quad (1)$$

where asterisk (*) indicates the convolution function, and the capitals indicate Fourier Transformation, and $D(\omega) = \sum_{k=-\infty}^{\infty} \delta(\omega - k\frac{2\pi}{T}) = \sum_{k=-\infty}^{\infty} \delta(\omega - \omega_k)$. The Fourier transform of the window function is seen to control the measured frequency content. Examples for several spectral windows are shown in Fig. 11. The phenomenon of 'spectral leakage' is clearly visible in this figure, where energy due to the non-periodic nature of the windowing process is migrated to higher-frequencies. In order to reduce the contribution of spectral leakage to the measured frequency content, it is common practice to taper the window function *w*, such that the side-lobes are smaller, invariably at the expense of losing some frequency resolution, but generally at the gain in amplitude resolution. Careful comparison of the properties of a large number of window functions is given in Heinzel *et al.* (2002), where the different windows are classified according to their ability to either resolve frequencies, as in the box-car window (Fig. 11a), resolve amplitudes, such as the flat-top windows (Fig. 11c), or be general purpose with some capability in both areas, such as the nutall windows (Fig. 11b). In this work we use the nutall4a window function of Heinzel *et al.* (2002) whose transform is displayed in Fig. 11b. This is a general-purpose window that has good amplitude and frequency resolution with side lobes that are around 100 dB below the main lobe. Note that it has become common practice in the literature to apply a fractionally tapered window to waveform data, so that, for example, only the first and last 10 % of the window function differs from unity. This can lead to significantly degraded behaviour and should be avoided. Figure 12 shows the window transform function for a window function that consists of a hanning taper applied to the first and last 10 % of the data.

Several additional concepts are important when considering the use of window functions as applied to the determination of Power Spectral Densities. The first of these is the notion of Incoherent Power Gain. The spatially-extended nature of the main lobe of the window transform function, generally extending across several frequency bins, allows the window to gather energy from those neighbouring bins. Harris (1978) shows that if N_0 is the noise-power per bin, then the total power P_w collected by the window function is $P_W = \frac{N_0}{2\pi}\int_{-\pi/\Delta}^{\pi/\Delta} |W(\omega)|^2 d\omega = \frac{N_0}{\Delta}\sum_{j=0}^{n-1} w_j^2 \equiv \frac{N_0}{\Delta} I_W$—where n is the number of samples, Δ is the sample rate, and I_W, which just is the sum of the squares of the window coefficients, is defined to be the Incoherent Power Gain of the window. We are therefore in a position to write an expression for the PSD of the finite-length digitally-sampled analogue signal $f(t)$. It is: $P_{\mathrm{SD}}(\omega_j) = \frac{2|F(\omega_j)|^2}{\Delta I_W}$—where $\omega_j = \frac{2\pi j}{n\Delta}$ for $j = 0, \ldots, n/2$, is the jth frequency picket, and F is the output of a unitary Fourier Transform algorithm. Here, we are taking into account the contribution of the negative frequencies with the factor 2. It is important to note that P is the power spectrum contained in each frequency bin, i.e., PSD, and not the power spectrum of an individual spectral component. To determine the power contained in an individual line spectra the concept of the Coherent Power Gain is useful. Application of Eq. (1) to the elemental waveform $f(t) = Ae^{i\omega_k t}$ yields the result.

$F(f(t)D(t)w(t)) = A\sum_{j=-\infty}^{\infty} w_j\delta(\omega - \omega_k) * \delta(\omega - \omega_j) = A\sum_{j=-\infty}^{\infty} w_j$, where w_j, are the values of the window function at times: $t + jT$ for $j = -\infty, \ldots, \infty$. In such a case, the Power Spectrum is given by $P_S(\omega_j) = \frac{2|F(\omega_j)|^2}{C_W}$, where C_W, which is the square of the sum of the window coefficients, is the Coherent Power Gain of the window. One can then estimate the amplitude of the line spectra by taking the square root of $P_S(\omega_j)$. The quantity β is known as the Equivalent Noise Bandwidth of the Window function and through straightforward multiplication allows one to convert *PSD* to *PS* and vice versa.

The Recommended Overlap Value (ROV) for the nutall4a window is 68 % (Heinzel *et al.*, 2002), implying a total of 63 three-min segments to be evaluated.

References

Bowman, J.R., Baker, G.E., and Bahavar, M, 2005. *Ambient infrasound noise*. Geophys Res. Lett. *32*. L09803, doi:10.1029/2005GL022486.

Bowman, J.R., Shields, G., O'Brien, M.S. 2007. *Infrasound Station Ambient Noise Estimates and Models 2003–2006* Infrasound Technology Workshop, Tokyo, 13–16, November 2007.

Bowman, J.R., Shields, G., O'Brien, M.S. 2009. Infrasound station ambient noise estimates and models 2003–2006 (Erratum), Infrasound Technology Workshop, Brasilia, Brazil, November 2–6, 2009.

Harris, F.J.,1978. *On the use of Windows for Harmonic Analysis with the Discrete Fourier Transform*. Proceedings of the IEEE *66* (1): 51–83. doi:10.1109/PROC.1978.10837.

Heinzel G., Rudiger, R., and Schilling R. 2002. Spectrum and spectral density estimation by the Discrete Fourier Transform (DFT), including a comprehensive list of window functions and some new flat-top windows. http://www.rssd.esa.int/SP/LISAPATHFINDER/docs/Data_Analysis/GH_FFT.pdf.

Lyons, R.G., 1997. "Understanding Digital Signal Processing", Addison-Wesley.

MATLAB, 2008. MATLAB version 7.7.0. Natick, Massachusetts: The MathWorks Inc.

McNamara, D.E. and R.P. Buland, 2004. *Ambient Noise Levels in the Continental United States*, Bull. Seism. Soc. Am., *94*, 4, 1517–1527.

McCauley, R.D., Jenner C., Bannister J.L., Burton C.L.K, Cato, D.H., and Duncan., A. 2001. Blue whale calling in the Rottnest trench—2000, Western Australia. Prepared for Environment Australia, from Centre for Marine Science and Technology, Curtin University, R2001–6, 55 pp.

Peterson, J., 1993. Observation and modeling of seismic background noise, U.S. Geol. Surv. Tech. Rept., 93–322, 1–95.

Richardson, W.J., Greene, C.R., Malme, C.I, and Thomson, D.H. 1995. *Marine Mamals and Noise*, Academic Press, San Diego. pp 576.

Schreier, P.J, and Scharf, L.L, 2010. Statistical signal processing of complex-valued data: the theory of improper and noncircular signals. *Cambridge University Press*. pp. 330.

Urick, R.J. 1984. *Ambient noise in the sea*. Report No. 20070117128. Undersea Warefare Technology Office, Naval Sea Systems Command, Department Of The Navy, Washington DC.

Welch, PD, 1967. The Use of Fast Fourier Transform for the Estimation of Power Spectra: A Method Based on Time Averaging Over Short, Modified Periodograms, IEEE Transactions on Audio Electroacoustics, Volume AU-15 pp. 70–73.

(Received September 30, 2011, revised August 6, 2012, accepted August 12, 2012, Published online September 8, 2012)